論文 / 著書情報
Article / Book Information

Title	Simulation and mitigation of the magneto-Rayleigh-Taylor instabilities in Z-pinch gas discharge extreme ultraviolet plasma radiation sources
Authors	B.Huang,T.Tomizuka,B.Xie,Y.Sakai,Q.Zhu,I.Song,A.Okino,F.Xiao,M.Watanabe,E.Hotta
Citation	Physics of Plasmas, Vol. 20, ,
Pub. date	2013, 11
URL	http://scitation.aip.org/content/aip/journal/pop
Copyright	Copyright (c) 2013 American Institute of Physics

Simulation and mitigation of the magneto-Rayleigh-Taylor instabilities in Z-pinch gas discharge extreme ultraviolet plasma radiation sources

B. Huang, T. Tomizuka, B. Xie, Y. Sakai, Q. Zhu et al.

Citation: Phys. Plasmas **20**, 112113 (2013); doi: 10.1063/1.4835275
View online: http://dx.doi.org/10.1063/1.4835275
View Table of Contents: http://pop.aip.org/resource/1/PHPAEN/v20/i11
Published by the AIP Publishing LLC.

Simulation and mitigation of the magneto-Rayleigh-Taylor instabilities in Z-pinch gas discharge extreme ultraviolet plasma radiation sources

B. Huang,[a] T. Tomizuka, B. Xie, Y. Sakai, Q. Zhu, I. Song, A. Okino, F. Xiao, M. Watanabe, and E. Hotta

Department of Energy Sciences, Tokyo Institute of Technology, 4259 J2-35 Nagatsuta, Midori-ku, Yokohama 226-8502, Japan

(Received 19 August 2013; accepted 11 November 2013; published online 26 November 2013)

The development and use of a single-fluid two-temperature approximated 2-D Magneto-Hydrodynamics code is reported. Z-pinch dynamics and the evolution of Magneto-Rayleigh-Taylor (MRT) instabilities in a gas jet type Extreme Ultraviolet (EUV) source are investigated with this code. The implosion and stagnation processes of the Z-pinch dynamics and the influence of initial perturbations (single mode, multi- mode, and random seeds) on MRT instability are discussed in detail. In the case of single mode seeds, the simulation shows that the growth rates for mm-scale wavelengths up to 4 mm are between 0.05 and 0.065 ns^{-1}. For multi-mode seeds, the mode coupling effect leads to a series of other harmonics, and complicates MRT instability evolution. For perturbation by random seeds, the modes evolve to longer wavelengths and finally converge to a mm-scale wavelength approximately 1 mm. MRT instabilities can also alter the pinch stagnation state and lead to temperature and density fluctuations along the Z axis, which eventually affects the homogeneity of the EUV radiation output. Finally, the simulation results are related to experimental results to discuss the mitigations of MRT instability. © *2013 AIP Publishing LLC*. [http://dx.doi.org/10.1063/1.4835275]

I. INTRODUCTION

Extreme Ultraviolet (EUV) lithography is considered to be the most promising candidate for the next generation lithography technology.[1] Laser Produced Plasma (LPP) sources and Discharge Produced Plasma (DPP) sources[2] are two prospective methods to produce the 13.5 nm EUV radiation sources. To date, insufficient source power[3] remains a critical issue for the High Volume Manufacturing (HVM) in EUV lithography. Z-pinch DPP plasmas[4–7] are efficient sources for the produce of high energy EUV radiation. In a Z-pinch, the pulsed current induces an azimuthal magnetic field so that the magnetic piston compresses the plasma column toward the axis, accompanied by a shock wave. The arrival of the shock front[8] at the axis marks the start of the stagnation phase, during which, the plasma kinetic energy is converted to thermal, ionization, and radiation energies.[8,9] The initial non-uniformity of the electron density in the plasma column is inevitable[10] because of the stochastic nature of the breakdown process. Z-pinches are thus inherently susceptible to Magneto-Rayleigh-Taylor (MRT) instabilities, especially for large-radius and long-time implosions. This instability[11,12] occurs at the plasma-magnetic piston interface and is believed to be capable of degrading implosion symmetry and limiting the Z-pinch source performance.[13] The HVM of EUV lithography requires the light source not only to have efficient output power but also to have high spatial stability, pulse-to-pulse energy stability, and a smaller spot size. It is therefore necessary to investigate the evolution of MRT instability and mitigation methods in order to design a suitable EUV radiation source.

Applying an axial magnetic field[10] or sheared flow[14–16] are effective ways to suppress the growth of the MRT instabilities. Our previous experiment[17] also shows that relatively lower dI/dt leads to asymmetric radiating plasma with larger spot size and lower EUV radiation output. Thus, a pulsed current with a faster rise time is preferred for DPP EUV sources. To provide better initial uniformity so as to mitigate the MRT instability, pre-ionization is necessary for Z pinch devices.[18] The Radio-Frequency (RF) pre-ionization system is used in our setup because it is an efficient method to generate a much denser pre-ionized plasma with high symmetry.[19]

Our work, reported here, is motivated by our recent experimental observation of MRT instabilities occurring in the gas discharge of the DPP EUV source. We have also developed a numerical code to investigate the MRT instabilities. In Sec. II, we present the Magneto-Hydrodynamics (MHD) model and the numerical scheme to solve the relevant equations. In Sec. III, we present the simulation results of the Z-pinch dynamics and discuss the characteristics of MRT instability in detail. The effects of different perturbation modes on MRT instability evolution are studied. In addition, we compare the simulation with experimental results and analyze the influences of MRT instability on pinch stagnation EUV radiation. Finally, our conclusions are given in Sec. IV.

II. NUMERICAL MODEL AND NUMERICAL SCHEME

The simulation is based on a two-dimensional axisymmetric MHD model in cylindrical geometry. We assume that the single-fluid, two-temperature plasma approximation is valid. The rate equations are coupled to the fluid equations, which take the collisional ionization, radiative recombination, and three-body recombination into account. The plasma

[a]Electronic addresses: huang.b.ab@m.titech.ac.jp and fanuc.huang@gmail.com

is assumed to be fully ionized and the equations are written in Gaussian units. The continuity equation is given by

$$\frac{\partial \rho}{\partial t} + \frac{1}{r}\frac{\partial (r\rho v_r)}{\partial r} + \frac{\partial (\rho v_z)}{\partial z} = 0, \quad (1)$$

where ρ is the plasma density, v_r is the velocity in the radial direction, and v_z is the velocity in the axial direction. The Navier-Stokes equations in both radial and axial directions read

$$\frac{\partial (\rho v_r)}{\partial t} + \frac{1}{r}\frac{\partial (r\rho v_r v_r)}{\partial r} + \frac{\partial p_{tot}}{\partial r} + \frac{\partial (\rho v_r v_z)}{\partial z} = -\frac{B^2}{4\pi r}, \quad (2)$$

$$\frac{\partial (\rho v_z)}{\partial t} + \frac{1}{r}\frac{\partial (r\rho v_z v_r)}{\partial r} + \frac{\partial ((\rho v_z v_z) + p_{tot})}{\partial z} = 0, \quad (3)$$

where $p_{tot} = p_e + p_i + p_{mag}$ is the total pressure, $p_e = n_e k_B T_e$ is the electron pressure, k_B is the Boltzmann constant, $p_i = n_i k_B T_i$ is the ion pressure, and $p_{mag} = B^2/(8\pi)$ is the magnetic pressure.

The electron and ion energy equations read

$$\frac{\partial E_e}{\partial t} + \frac{1}{r}\frac{\partial (r v_r (E_e + p_e))}{\partial r} + \frac{\partial (v_z (E_e + p_e))}{\partial z} = Q_j + Q_{th,e} - Q_{brem} - Q_{ei} - Q_{atom}, \quad (4)$$

$$\frac{\partial E_i}{\partial t} + \frac{1}{r}\frac{\partial (r v_r (E_i + p_i))}{\partial r} + \frac{\partial (v_z (E_i + p_i))}{\partial z} = Q_{th,i} + Q_{ei}, \quad (5)$$

where $E_e = \frac{3}{2} n_e k_B T_e$ is the electron internal energy and $E_i = \frac{3}{2} n_i k_B T_i$ is the ion internal energy. The Joule heating is

$$Q_j = \frac{c^2 \eta}{16\pi^2} (\nabla \times \vec{B}) \times \vec{B},$$

where η is the Spitzer resistivity.[20] The electron or ion thermal diffusions are

$$Q_{th,e/i} = \nabla \lambda_{e/i} \nabla T_{e/i},$$

where $\lambda_{e/i}$ is the thermal conductivity of the electron or ion, respectively. Q_{brem} is the energy loss through Bremsstrahlung radiation,[20] Q_{ei} is the electron-ion energy exchange,[21] and Q_{atom} is the energy loss in atomic processes, including collisional ionization, radiative recombination, and three-body recombination.

The magnetic induction equation, neglecting the time variation of the electric field,[22] reads

$$\frac{\partial \vec{B}}{\partial t} + \frac{\partial (v_r \vec{B})}{\partial r} + \frac{\partial (v_z \vec{B})}{\partial z} = -\frac{c^2}{4\pi} \nabla \times (\eta \nabla \times \vec{B}). \quad (6)$$

The rate equations is given by

$$\frac{dn_{Z+1}}{dt} = n_e n_Z S(Z, Te) - n_e n_{Z+1} (S(Z+1, Te) + \alpha_r (Z+1, Te) + n_e \alpha_{3b} (Z+1, Te)) + n_e n_{Z+2} (\alpha_r (Z+2, Te) + n_e \alpha_{3b} (Z+2, Te)), \quad (7)$$

where S is the collisional ionization rate coefficient, α_r is the radiative recombination rate coefficient, and α_{3b} is the three-body recombination rate coefficient.

The governing equations discussed above are numerically solved by the Total Variation Diminishing (TVD) scheme,[23] a well known high-resolution compressible fluid dynamics procedure, which has become widely accepted for practical applications. In the TVD scheme, a nonlinear numerical limiter is devised to switch the spatial discretization between a monotonic scheme that satisfies the entropy condition and a high-order scheme. This switching eliminates spurious numerical oscillations in the presence of discontinuities while retaining the high order accuracy for smooth solutions. For the hyperbolic flux function, we make use of Lax-Friedrich (LF) splitting,[24] which is one of the most robust approximate Riemann solvers for hyperbolic systems. The TVD-LF scheme has been demonstrated to be accurate and efficient for MHD problems.[25] The diffusion terms are treated separately to ensure the stability of the calculation. The derivation of the time step for the MHD problem was given by Toth *et al.*,[26] and is mainly restricted by the plasma diffusion time scale rather than the convection-dominated processes of fluid dynamics.

Due to axial symmetry, the boundary conditions on axis ($r = 0$) are $\frac{\partial T_i}{\partial r} = \frac{\partial T_e}{\partial r} = 0$, $B = 0$, $\frac{\partial v_z}{\partial r} = 0$, and $v_r = 0$. At the outer boundary ($r = r_0 = 0.3$ cm), the magnetic field is given as

$$B = \frac{2I}{r_0 \cdot c},$$

where the current waveform $I = I_0 \sin(\omega t)$, here, $I_0 = 22$ kA and $\omega = 1 \times 10^7$ rad s^{-1}. $\frac{\partial v_r}{\partial r} = \frac{\partial v_z}{\partial r} = 0$. Periodic boundary conditions are imposed on $z = 0$ and $z = 6$ mm.

In this paper, we assume that the initial distribution of the plasma is uniform and at Local Thermodynamic Equilibrium (LTE). This simplification is sufficient for the essentials of Z-pinch dynamics and for the evolution of MRT instabilities to be grasped. The initial Xenon (Xe) ion density is assumed to be $n_0 = 2 \times 10^{16}$ cm^{-3}, and the initial electron and ion temperatures $T_e = T_i = 1$ eV. Under such circumstance, the number density of Xe^{2+} or higher charge states is negligible compared with Xe^{1+}.

III. RESULTS AND DISCUSSION

A. Z-pinch dynamics

During the implosion phase, the high temperature of the compressed plasma ahead of the piston produce a high pressure region, which leads to the formation of a shock wave. The plasma shell becomes denser as it accumulates, and also obtain kinetic energy through $\vec{J} \times \vec{B}$. We denote the position of the shock front, r_s, to be at the ion density maximum and the magnetic piston position, r_p, to be at the magnetic field maximum. Fig. 1 shows r_s and r_p as a function of time without initial perturbation. The shock front reaches the Z axis at 203 ns, ahead of the magnetic piston. This moment is the beginning of pinch stagnation. The shock front reflects at about 210 ns, having stagnated on the axis for several nanoseconds, while the magnetic piston continues to compress the plasma. At 241 ns, the shock front again turns back toward the axis. There is an abrupt decrease of r_p near 240 ns shown in the

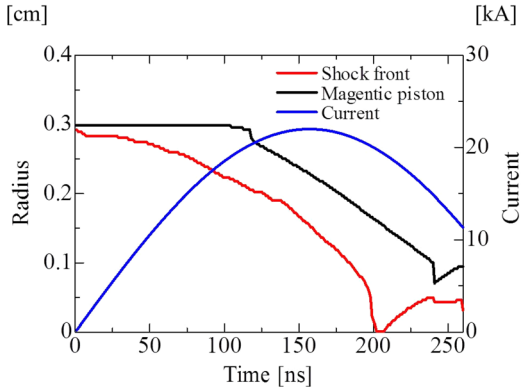

FIG. 1. Position of shock front (r_s), magnetic piston (r_p) as a function of time without initial perturbation.

figure. This is because r_p is defined as the maximum magnetic field position and is thus particularly sensitive to the magnetic field radial profile. In this simulation, the radial profile is double peaked; for $t \leq 240$ ns, the outer peak is but for $t \geq 241$ ns, the inner peak becomes dominant. This caused the abrupt change, in this case a decrease in radial position, of the defined maximum magnetic field position and thus r_p.

Fig. 2 shows the on axis electron temperature, electron density, ion temperature, and ion density as a function of time without initial perturbation. The electron and ion temperatures increase significantly immediately before stagnation, as is shown in Fig. 2(a). This is due to the combined effect of adiabatic heating and energy transfer from kinetic to internal energy. During pinch stagnation, the electron and ion densities are high enough (Fig. 2(b)) for sufficient electron-ion collisions to occur, so that the temperature difference between electrons and ions becomes small. $T_e \approx T_i$ at about 220 ns. High temperature and high density conditions are necessary to produce EUV radiation at pinch stagnation. The optimum electron temperature and density for 13.5 nm EUV emission from Xe plasmas are $25 \sim 30$ eV and $10^{18} \sim 10^{19}$ cm^{-3}, respectively.[27] Although the electron temperature in this figure is higher than the optimum at stagnation, it is tunable by changing the initial density distribution.

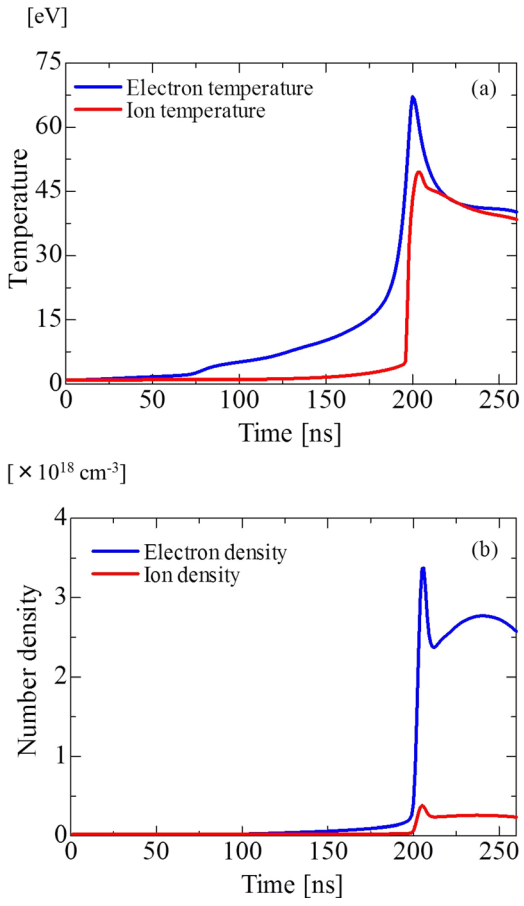

FIG. 2. On axis electron and ion temperatures (a), electron and ion densities (b), as a function of time without initial perturbation.

B. MRT instability simulations

MRT instability is an inherent problem for Z-pinches. In this section, we focus on the simulation of a Z-pinch with a uniform initial density distribution on which perturbations are superimposed. The density perturbation for the single mode is given by

$$\rho = \rho_0 \left(1 + \delta \cdot \cos\left(\frac{2\pi}{\lambda} \cdot z\right)\right),$$

where δ is the initial perturbation amplitude, λ is the wavelength of the perturbation, and ρ_0 is the unperturbed density. The multi-mode perturbation is a superposition of single mode perturbations.

Fig. 3 shows an example of ion density evolution with initial multi-mode perturbation wavelengths of $\lambda = 0.75$ mm, $\lambda = 1.5$ mm, and $\lambda = 3$ mm at (a) 145 ns, (b) 223 ns, and (c) 260 ns, respectively. The initial perturbation amplitude is $\delta = 0.1$. The simulation shows that the shock front is MRT stable during the implosion phase (t = 145 ns); while the region between shock front and magnetic piston is MRT unstable. The shock front remains stable even after it is reflected from the axis (t = 223 ns), whereas the magnetic piston region is severely perturbed. Shortly after, the magnetic piston arrives and interacts with the reflected shock indirectly at $r \sim 0.1$ cm. The turbulent motion is therefore transferred from the magnetic piston to the stagnated plasma[28] and perturbs the plasma column. The shell thickness is on the order of 1 mm, which is important for later discussion.

1. Single mode seeds

To better understand the evolution of the MRT instability, we simulate perturbations of single mode, multi-modes, and random modes, respectively. The Fast Fourier Transform (FFT) is often used to analyze the characteristics of the MRT instability.[12,29] Fig. 4 shows the normalized FFT spectrum at the plasma-magnetic piston interface, r_p, with $\lambda = 1.5$ mm and $\delta = 0.1$ at 1 ns, 75 ns, 170 ns, and 205 ns, respectively, for a single mode perturbation. Initially, only the fundamental harmonic originating from the single mode seeds is present. The second harmonic appears after 75 ns, declaring the end of the linear regime as the MRT instability

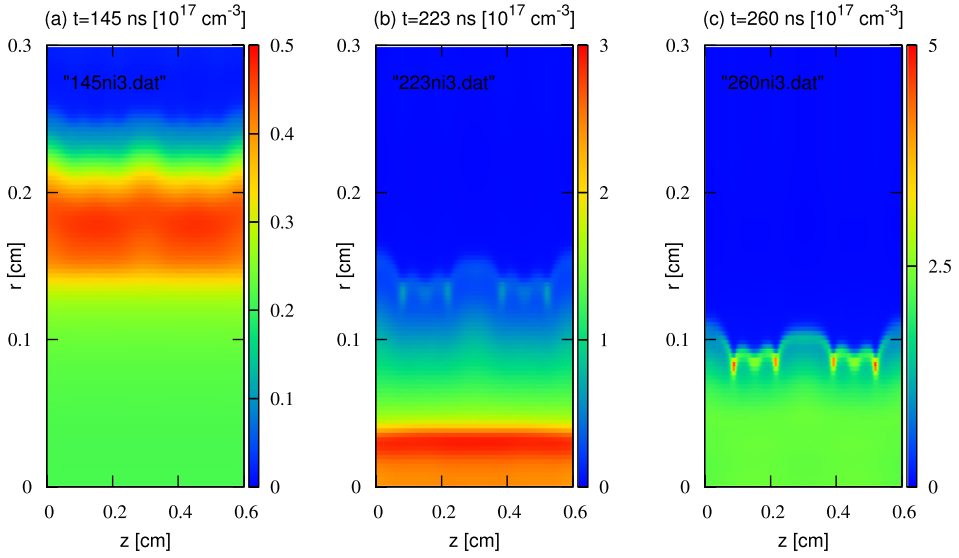

FIG. 3. Ion density distribution during implosion with an initial multi-mode perturbation amplitude of 0.1 and wavelengths of $\lambda = 0.75$ mm, $\lambda = 1.5$ mm, and $\lambda = 3$ mm at (a) 145 ns, (b) 223 ns, and (c) 260 ns.

enters the weak non-linear regime. As the MRT instability evolves, the third ($t = 170$ ns) and higher order harmonics ($t = 205$ ns) appear, indicating the MRT instability reaching the deep non-linear regime.

According to classical linear theory, the fundamental harmonic grows exponentially in the linear regime. Douglas *et al.*[12] point out that the growth rate may remain in the exponential form after the onset of nonlinear development. Fig. 5(a) shows the fundamental amplitude as a function of time and its exponential fit for $\lambda = 1.5$ mm and $\delta = 0.1$. The growth rate is $\gamma = 0.05\ \text{ns}^{-1}$. In the final stage, the fundamental amplitude deviates from the exponential fit, indicating a much faster growth rate than in the linear regime. The growth rates for mm-scale perturbations up to 4 mm are shown in Fig. 5(b), to be from $\sim 0.05\ \text{ns}^{-1}$ to $0.065\ \text{ns}^{-1}$.

2. Multi-mode seeds

For multi-mode perturbation structures, the mode coupling effect becomes much more significant and further complicates the MRT evolution. Fig. 6(a) shows the spectral

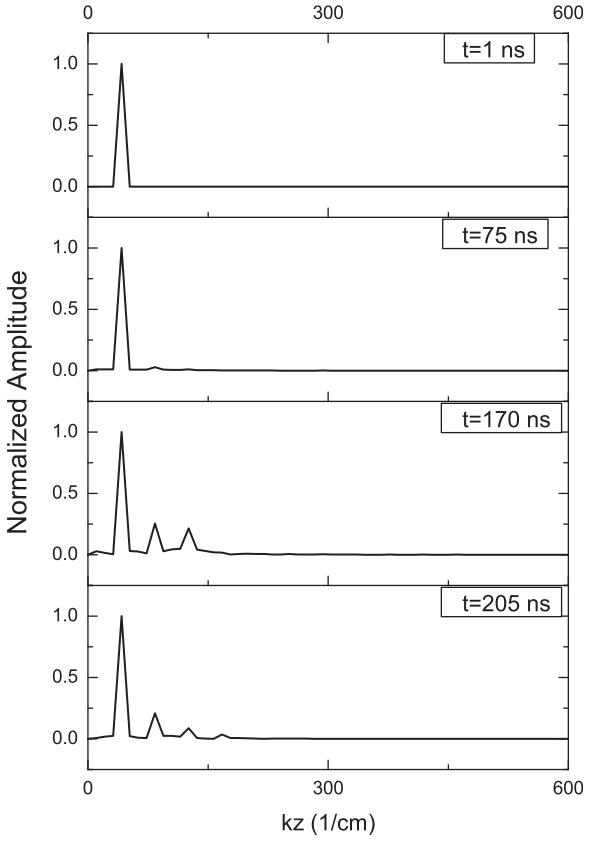

FIG. 4. FFT spectrum of perturbation amplitude ($\lambda = 1.5$ mm) and $\delta = 0.1$ at 1 ns, 75 ns, 170 ns, and 205 ns, respectively.

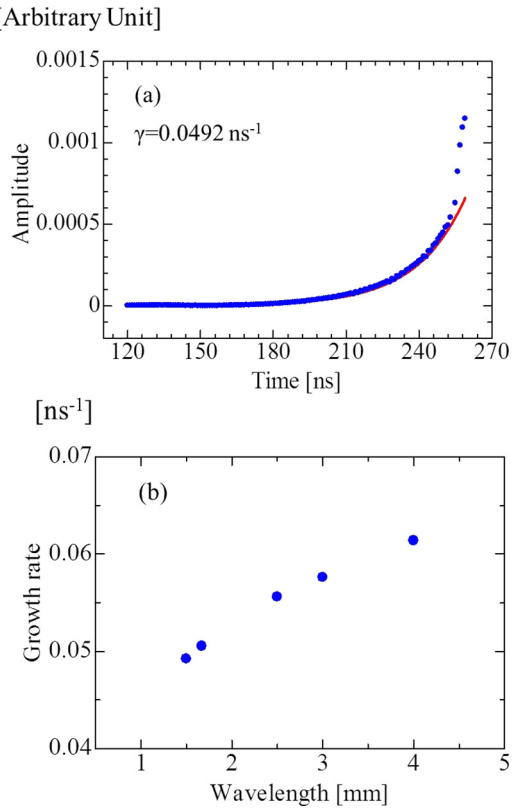

FIG. 5. Time evolution of the fundamental FFT spectrum amplitude and its exponential fit for $\lambda = 1.5$ mm and $\delta = 0.1$ (a), and growth rate of the fundamental harmonic versus mm-scale wavelengths (b).

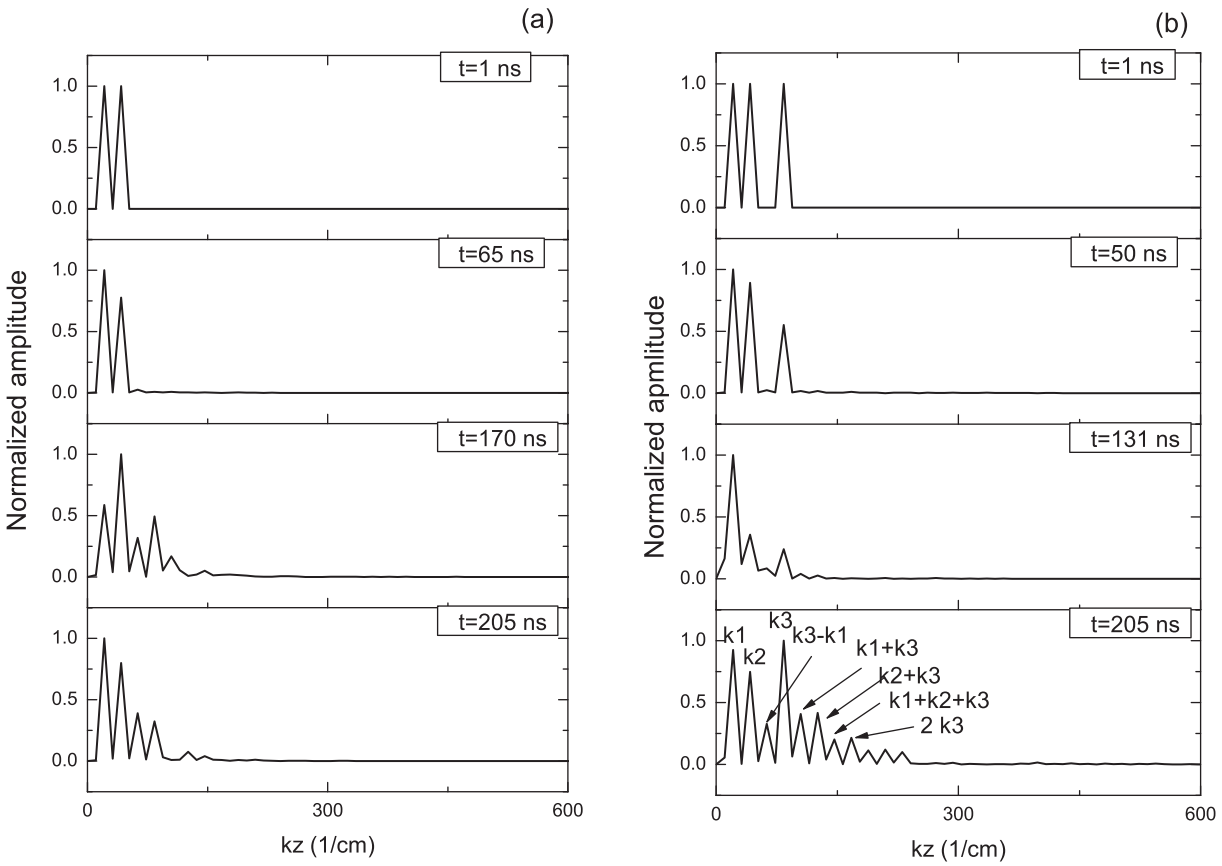

FIG. 6. The temporal evolution of multi-mode structure FFT spectrum. (a) two-mode structure with $\lambda = 1.5$ mm and $\lambda = 3$ mm at 1 ns, 65 ns, 170 ns, and 205 ns; (b) three-mode structure with $\lambda = 0.75$ mm, $\lambda = 1.5$ mm, and $\lambda = 3$ mm at 1 ns, 50 ns, 148 ns, and 205 ns. The perturbation amplitude is $\delta = 0.1$.

evolution of a two-mode structure comprised of $\lambda = 1.5$ mm and $\lambda = 3$ mm; and Fig. 6(b) shows the spectral evolution of a three-mode structure comprised of $\lambda = 0.75$ mm, $\lambda = 1.5$ mm, and $\lambda = 3$ mm, respectively. The perturbation amplitude is $\delta = 0.1$. During the initial stage($t = 1$ ns), only fundamental harmonics are present and their amplitudes are equal. During the implosion phase, other harmonics are induced due to the mode coupling effect. At 205 ns, the mode coupling effect becomes so significant that the amplitudes of some induced modes reach more than 30% of the fundamental modes amplitudes. In the case of the three-mode structure, we can see a series of modes generated, including k3 − k1, k1 + k3, k2 + k3, k1 + k2 + k3, amongst others. In this situation, a severe bubble-and-spike structure is formed near the plasma-magnetic piston interface, as shown in Fig. 3. The lower density and larger local magnetic field cause high acceleration in the bubble regions between spikes, and also cause the severe perturbation observed. The magnetic field diffuses through the spike regions so that the driving forces reside at the bubble front, elongating the spikes.[12]

3. Random seeds

Random density seeds[30–33] have been used to model the MRT instability in Z-pinches and shown good agreement with experimental results. The random seeds can be decomposed into a series of single mode seeds. The density perturbation for the random seeds is given by

$$\rho = \rho_0(1 + \delta \cdot Random\_Number),$$

where the initial amplitude $\delta = 0.05$ and *Random_Number* is a random number between −1 and 1. The spectral evolution of the random seeds perturbation at (a) 1 ns, (b) 50 ns, (c) 170 ns, and (d) 205 ns are shown in Fig. 7. In the initial stage (t = 1 ns), the FFT spectrum is distributed over a wide range of wave numbers. As the Z pinch evolves (t = 50 ns), the shorter wavelength modes gradually vanish, and longer wavelength amplitudes increase. In the final image (t = 205 ns), the dominant modes are $k1 = 12.27\ \mathrm{cm}^{-1}$, $k2 = 61.34\ \mathrm{cm}^{-1}$, and $k3 = 85.9\ \mathrm{cm}^{-1}$, corresponding to wavelengths of 5.12 mm, 1.02 mm, and 0.73 mm, respectively. The most dominant wavelength is $\lambda = 1.02$ mm. In our case, the thickness of the imploding plasma shell is on the order of 1 mm, as shown in Fig. 3. For perturbations with wavelengths that are shorter than the shell thickness, growth is inhibited because magnetic field contours cannot conform to the distorted surface.[34] On the other hand, the modes with wavelengths longer than this value are still growing. Furthermore, modes may be coupled and contribute to neighboring ones so that the final spectrum profile is modified. Hussey *et al.*[34] point out that the final dominant wavelength are on the order of shell thickness of the imploding plasma, which is determined by magnetic field diffusion. Note that in our random seeds simulation, the perturbation evolves to mm-scale wavelengths with a dominant wavelength of 1.02 mm.

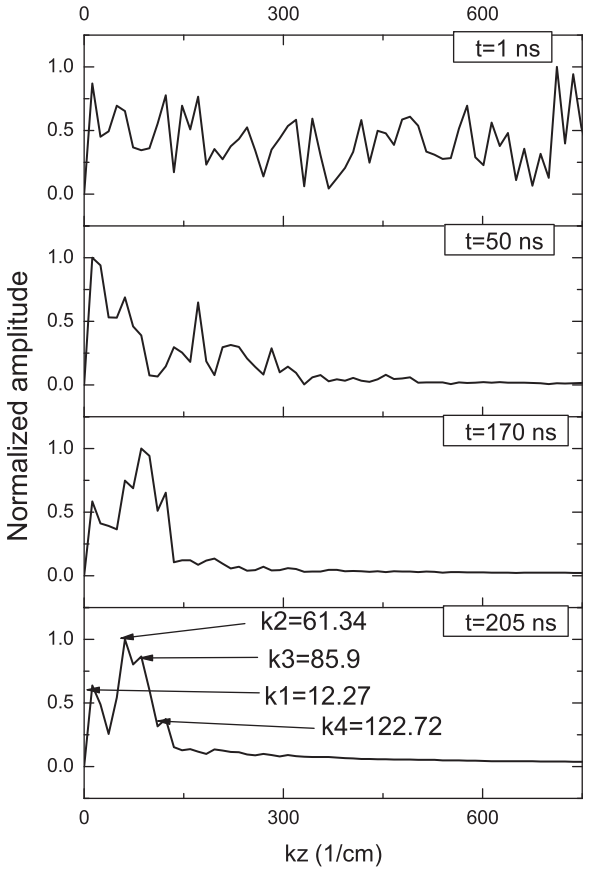

FIG. 7. FFT spectrum of the MRT instability with random seeds for initial perturbation amplitude $\delta = 0.05$.

4. Comparison with experimental results

The MRT instability is also observed in our Z-pinch gas discharge experiment. The experiment is based on an RF gas jet type Xe DPP EUV setup.[35] A pulsed power supply was designed which can provide a current pulse with peak value of about 22 kA with a rise time of about 110 ns. The power supply consists of a trigger system, an LC inversion circuit, a 1:3 step-up transformer, and a two-stage magnetic pulse compression circuit. The Xe gas is first pre-ionized by the RF coil with a working frequency of 13.56 MHz and then supplied to the main discharge chamber. The EUV emission is recorded with Si/Zr coated photodiode (IRD AXUV20HS1). A detailed description is given in Ref. 35. An X-ray CCD camera, a 50 μm diameter pinhole, and a Zr filter ($7 \sim 16$ nm) are assembled to form a pinhole imaging system to record the time-integrated EUV image. The pinhole image diagnostics system and the observation region are shown in Fig. 8. d indicates the distance from the RF coil to the cathode.

The time-integrated EUV pinhole image for an input gas pressure of 24 Torr and $d = 50$ cm is shown in Fig. 9. When weak pre-ionization (10 W) is applied, the EUV radiating column at stagnation suffers from instability. The wavelength of the instability is about 1 mm, consistent with our random seeds simulation. The inhomogeneity of the pinched plasma column causes two bright spots, which is undesirable for EUV source design. When the RF power is raised to 30 W, the initial uniformity of the plasma is improved so that the instability is suppressed. By further increasing the RF

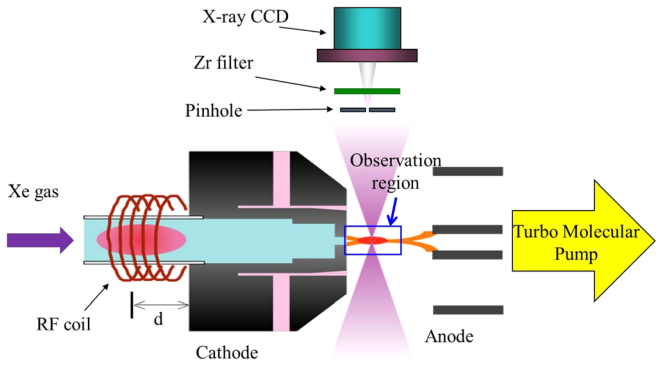

FIG. 8. Electrode structure and time-integrated EUV pinhole diagnostics system of the Z-pinch DPP source. d indicates the distance from the RF coil to the cathode.

power, the MRT instability is completely mitigated and a homogeneous pinched plasma column is formed. However, the peak EUV radiation intensity decreases at the same time.

By changing the distance d, the EUV pinhole images differ significantly under fixed input gas pressure of 24 Torr and fixed RF power of 10 W, as shown in Fig. 10. For $d = 20$ cm, the RF coil is close to the cathode, and sustains a uniform initial plasma distribution; therefore, the pinched plasma at stagnation is relatively homogeneous. The MRT instability appears when d increases. Note that the final dominant wavelength of the MRT instability always remains

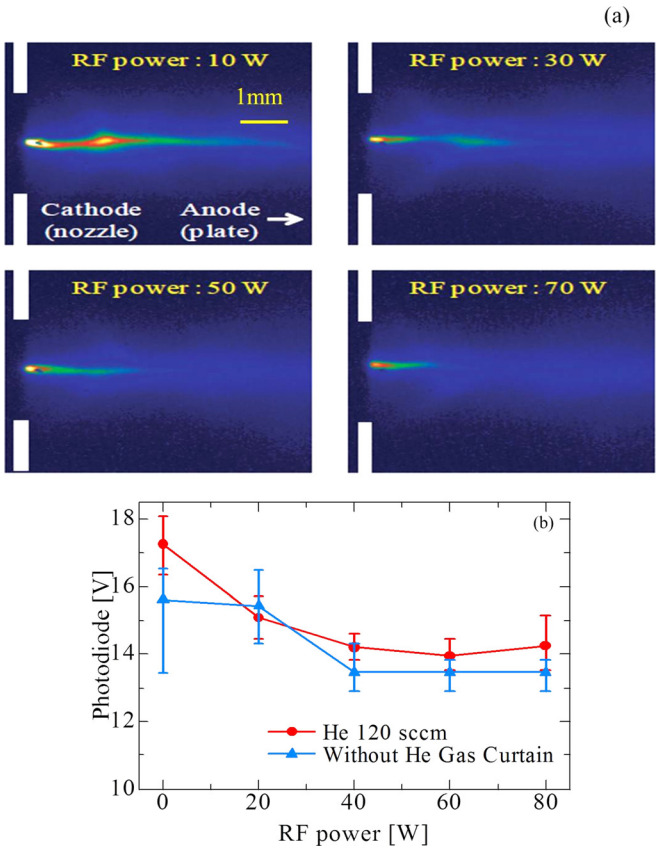

FIG. 9. (a) Time-integrated EUV pinhole image near the cathode region with pre-ionization powers of 10 W, 30 W, 50 W, and 70 W, respectively. (b) The EUV output power as a function of RF power with and without RF pre-ionization. The input gas pressure is fixed at 24 Torr and the distance from the RF coil to the electrode d = 50 cm.

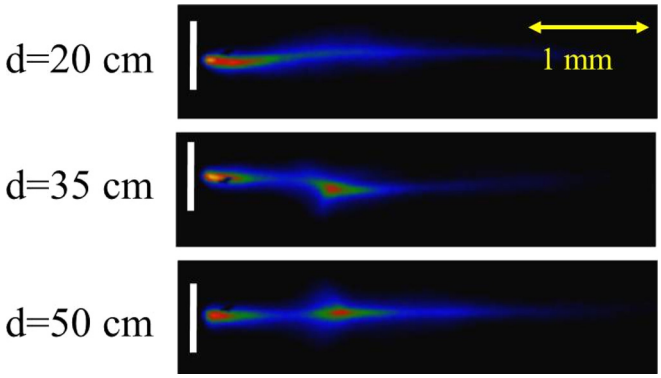

FIG. 10. EUV pinhole image versus the distance from RF coil to electrode of $d = 20$ cm, 35 cm, and 50 cm, respectively. The input gas pressure is fixed at 24 Torr and the RF power is 10 W.

around 1 mm. As discussed in the random seeds simulation Sec. III B 3, this characteristic wavelength is determined by the shell thickness of the imploding plasma.

The influence of the MRT instability on pinch stagnation is important to determine the EUV radiation output. Fig. 11 shows the simulation results of on axis electron temperature and density at pinch stagnation. For single mode perturbation, the on axis electron temperature fluctuation is more pronounced at longer initial perturbation wavelengths than at shorter wavelengths, as shown in Fig. 11(a). The MRT

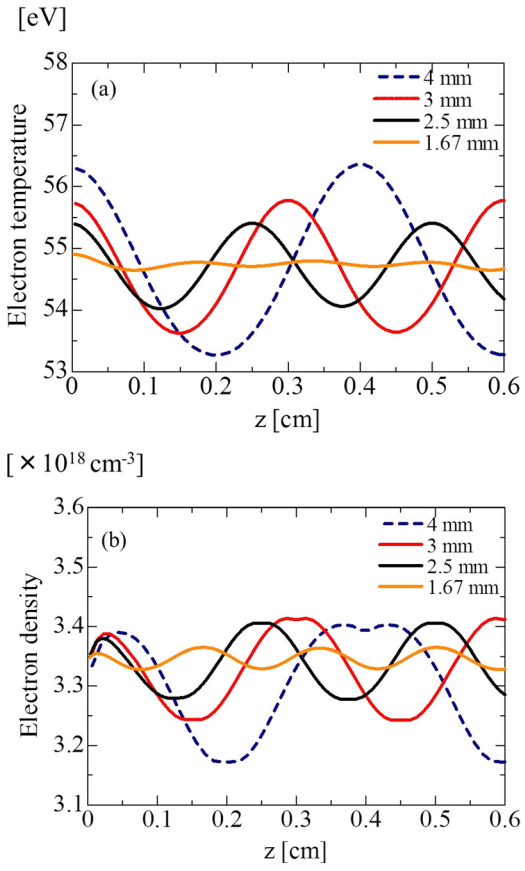

FIG. 11. On axis distribution of electron temperature and density at stagnation (t = 207 ns). (a) Single mode on axis electron temperature distribution with wavelengths of 4 mm, 3 mm, 2.5 mm, and 1.67 mm. (b) Single mode on axis electron density distribution with wavelengths of 4 mm, 3 mm, 2.5 mm, and 1.67 mm.

instability stems from the plasma-magnetic piston interface and has a sinusoidal profile. This type of density profile causes non-uniformity of the Lorentz force distribution. Thus, the pinched plasma column also has an axial density fluctuation, which is more obvious for longer wavelength perturbations. In the neck region, the plasma volume is compressed to a smaller radius and the magnetic field is stronger; a higher density and temperature region is thus formed at the shock front by adiabatic compression. The temperature fluctuation is about 3.5 eV for a $\lambda = 4$ mm perturbation. Such a fluctuation would significantly alter the 13.5 nm EUV generation because the optimum electron temperature is between 25 eV and 30 eV, and thus has a span of only 5 eV. On the other hand, in Fig. 11(b), while the on axis electron density distribution also fluctuates, it does not exceed the optimum electron density range (10^{18} to 10^{19} cm^{-3}). Therefore, the main reason for the non-uniformity of the EUV radiation at stagnation is the temperature fluctuation caused by the MRT instability.

RF pre-ionization can inhibit the amplitude of instabilities,[18] and so contribute to MRT instability suppression in Z-pinches. Fig. 12 shows the simulation results of the peak to peak electron density and temperature fluctuations versus initial perturbation amplitude, for $\lambda = 3$ mm at pinch stagnation. The on-axis fluctuations of both temperature and density are almost proportional to the initial amplitude; that is to say that the uniformity at pinch stagnation is improved by decreasing the initial amplitude. Double bright spots are observed in the pinhole imaging experiment with RF power of 10 W, as shown in Fig. 9(a), because the instability causes the local temperature to be higher and satisfies the optimum condition. By increasing the RF pre-ionization power, the initial amplitude of instabilities is inhibited so that more uniform pinched plasma column can be formed. On the other hand, the temperature fluctuation at stagnation is also suppressed and temperature at those spots is reduced below the optimum range, therefore, the EUV radiation output decreases.

In our previous experiment,[17] increasing dI/dt was shown to be an effective method to enhance the stability of the Z-pinch EUV source. By increasing dI/dt, the shell thickness of the imploding plasma becomes thinner, thus shortening the

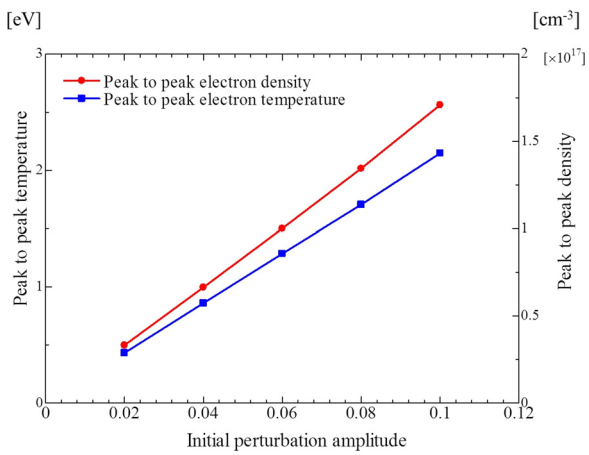

FIG. 12. Peak to peak electron density and temperature fluctuation versus initial amplitude for $\lambda = 3$ mm single mode perturbation at pinch stagnation.

final dominant wavelength of the instability. As shown in Fig. 11, shorter wavelength leads to smaller temperature and density fluctuations at the stagnation phase, which can improve the uniformity of the pinched plasma column. Katsuki *et al.*[36] also show that applying an axial magnetic field can suppress the MRT instability and reduce the pinched plasma temperature; therefore, the EUV radiation spectrum shifts to longer wavelengths. An adequate axial magnetic field ($B_z = 170$ G in Katsuki's case) can enhance the EUV radiation. However, EUV radiation output decreases if the axial magnetic field is too strong because the pinched plasma temperature may below the optimum range. Future work should be focused on both mitigating the MRT instability and improving the EUV radiation output.

IV. CONCLUSIONS

Z-pinch is an efficient method to produce high temperature and high density plasma sources for EUV lithography. The MRT instability is an inherent problem that affects the uniformity and output power of EUV radiation. Here, a 2-D MHD code was developed to investigate the MRT instability and its influences on EUV radiation. The typical growth rate for mm-scale wavelengths is from 0.05 to 0.065 ns^{-1}. Mode coupling effect was demonstrated to cause the generation of new modes, which were more pronounced for multi-mode and random seeds. The tendency for instability to converge to mm-scale wavelengths around 1 mm was validated both experimentally and numerically. The instability leads to temperature and density fluctuations along the Z axis at pinch stagnation. Due to the fluctuations, the radiation at the stagnation phase becomes inhomogeneous. Instability mitigation technologies, including RF pre-ionization, increasing dI/dt, and applying an axial magnetic field, have also been discussed.

[1]B. Wu and A. Kumar, *Extreme Ultraviolet Lithography* (McGraw-Hill, New York, 2009).
[2]V. Bakshi, *EUV Sources for Lithography* (SPIE, Bellingham, Washington, 2006).
[3]V. Banine, S. Young, and R. Moores, "EUV Lithography: today and tomorrow," in *Proceedings of 2012 International Workshop on EUV and Soft X-ray Sources*, Dublin, Ireland, 8–12 October 2012.
[4]K. Bergmann, G. Schriever, O. Rosier, M. Mller, W. Neff, and R. Lebert, "Highly repetitive, extreme-ultraviolet radiation source based on a gas-discharge plasma," Appl. Opt. **38**, 5413 (1999).
[5]U. Stamm, "Extreme ultraviolet light sources for use in semiconductor lithography: state of the art and future development," J. Phys. D **37**, 3244 (2004).
[6]V. M. Borisov, A. V. Eltsov, A. S. Ivanov, Y. B. Kiryukhin, O. B. Khristoforov, V. A. Mishchenko, A. V. Prokofiev, A. Y. Vinokhodov, and V. A. Vodchits, "EUV sources using Xe and Sn discharge plasmas," J. Phys. D **37**, 3254 (2004).
[7]I. V. Fomenkov, N. Bwering, C. L. Rettig, S. T. Melnychuk, I. R. Oliver, J. R. Hoffman, O. V. Khodykin, R. M. Ness, and W. N. Partlo, "EUV discharge light source based on a dense plasma focus operated with positive and negative polarity," J. Phys. D **37**, 3266 (2004).
[8]D. D. Ryutov, M. S. Derzon, and M. K. Matzen, "The physics of fast Z pinches," Rev. Mod. Phys. **72**, 167 (2000).
[9]E. Kroupp, D. Osin, A. Starobinets, V. Fisher, V. Bernshtam, L. Weingarten, Y. Maron, L. Uschmann, E. Forster, A. Fisher, M. E. Cuneo, C. Deeney, and J. L. Giuliani, "Ion temperature and hydrodynamic-energy measurements in a Z-pinch plasma at stagnation," Phys. Rev. Lett. **107**, 105001 (2011).
[10]M. A. Liberman, J. S. De Groot, A. Toor, and R. B. Spielman, *Physics of High-Density Z-Pinch Plasmas* (Springer, New York, 1999).
[11]Y. Zhang, W. Jiming, D. Zihuan, D. Ning, N. Cheng, Y. Yanzhong, X. Delong, S. Shunkai, G. Tongxiang, C. Yi, H. Jun, X. Chuang, and S. Xiaojian, "Computational investigation of the magneto-Rayleigh-Taylor instability in Z-pinch implosions," Phys. Plasmas **17**, 042702 (2010).
[12]M. R. Douglas, C. Deeney, and N. F. Roderick, "Computational investigation of single mode vs multimode Rayleigh-Taylor seeding in Z-pinch implosions," Phys. Plasmas **5**, 4183 (1998).
[13]J. S. De Groot, A. Toor, S. M. Golberg, and M. A. Liberman, "Growth of the Rayleigh-Taylor instability in an imploding Z-pinch," Phys. Plasmas **4**, 737 (1997).
[14]U. Shumlak and N. F. Roderick, "Mitigation of the Rayleigh-Taylor instability by sheared axial flows," Phys. Plasmas **5**, 2384 (1998).
[15]U. Shumlak and N. F. Roderick, "Sheared flow stabilization of the m = 1 kink mode in Z pinches," Phys. Rev. Lett. **75**, 3285 (1995).
[16]T. D. Arber and D. F. Howell, "The effect of sheared axial flow on the linear stability of the Zpinch," Phys. Plasmas **3**, 554 (1996).
[17]I. Song, K. Iwata, Y. Homma, S. R. Mohanty, M. Watanabe, T. Kawamura, A. Okino, K. Yasuoka, K. Horioka, and E. Hotta, "A comparative study on the performance of a xenon capillary Z-pinch EUV lithography light source using a pinhole camera," Plasma Sources Sci. Technol. **15**, 322 (2006).
[18]E. Ruden, H. U. Rahman, A. Fisher, and N. Rostoker, "Stability enhancement of a low initial density hollow gas-puff z pinch by e^- beam preionization," J. Appl. Phys. **61**, 1131 (1987).
[19]M. McGeoch, "Radio-frequency-preionized xenon z-pinch source for extreme ultraviolet lithography," Appl. Opt. **37**, 1651 (1998).
[20]L. Spitzer, *Physics of Fully Ionized Gases*, 2nd ed. (Interscience Publishers, New York, 1962).
[21]D. Duchs and H. R. Griem, "Computer study of the dynamic phase of a small θ pinch," Phys. Fluids **9**, 1099 (1966).
[22]N. H. Burnett and A. A. Offenberger, "Magnetohydrodynamic behavior of a laser-heated solenoid," J. Appl. Phys. **45**, 2155 (1974).
[23]A. Harten, "High-resolution schemes for hyperbolic conservation-laws," J. Comput. Phys. **49**, 357 (1983).
[24]C. W. Shu and S. Osher, "Efficient implementation of essentially non-oscillatory shock-capturing schemes," J. Comput. Phys. **77**, 439 (1988).
[25]G. Toth and D. Odstrcil, "Comparison of some flux corrected transport and total variation diminishing numerical schemes for hydrodynamic and magnetohydrodynamic problems," J. Comput. Phys. **128**, 82 (1996).
[26]G. Toth, R. Keppens, and M. A. Botchev, "Implicit and semi-implicit schemes in the versatile advection code: numerical tests," Astron. Astrophys. **332**, 1159 (1998); see http://aa.springer.de/papers/8332003/2301159.pdf.
[27]N. Bowering, M. Martins, W. N. Partlo, and I. V. Fomenkov, "Extreme ultraviolet emission spectra of highly ionized xenon and their comparison with model calculations," J. Appl. Phys. **95**, 16 (2004).
[28]H. R. Strauss, "Stagnation of a gas puff Z pinch," Phys. Plasmas **19**, 032705 (2012).
[29]M. R. Douglas, J. S. De Groot, and R. B. Spielman, "The magneto-Rayleigh-Taylor instability in dynamic z pinches," Laser Part. Beams **19**, 527 (2001).
[30]D. L. Peterson, R. L. Bowers, J. H. Brownell, A. E. Greene, K. D. McLenithan, T. A. Oliphant, N. F. Roderick, and A. J. Scannapieco, "Two-dimensional modeling of magnetically driven Rayleigh-Taylor instabilities in cylindrical Z pinches," Phys. Plasmas **3**, 368 (1996).
[31]R. L. Bowers, G. Nakafuji, A. E. Greene, K. D. McLenithan, D. L. Peterson, and N. F. Roderick, "Two-dimensional modeling of x-ray output from switched foil implosions on Procyon," Phys. Plasmas **3**, 3448 (1996).
[32]J. H. Hammer, J. L. Eddleman, P. T. Springer, M. Tabak, A. Toor, K. L. Wong, G. B. Zimmerman, C. Deeney, R. Humphreys, T. H. Nash, T. W. L. Sanford, R. B. Spielman, and J. S. De Groot, "Two-dimensional radiation magnetohydrodynamic simulations of SATURN imploding Z pinches," Phys. Plasmas **3**, 2063 (1996).
[33]M. R. Douglas, C. Deeney, and N. F. Roderick, "Effect of sheath curvature on Rayleigh-Taylor mitigation in high-velocity uniform-fill, Z-Pinch implosions," Phys. Rev. Lett. **78**, 4577 (1997).
[34]T. W. Hussey, N. F. Roderick, U. Shumlak, R. B. Spielman, and C. Deeney, "A heuristic model for the nonlinear Rayleigh-Taylor instability in fast Z pinches," Phys. Plasmas **2**, 2055 (1995).
[35]B. Huang, Y. Takimoto, M. Watanabe, and E. Hotta, "Effect of electron density on extreme ultraviolet output of a Z-pinch Xe discharge produced plasma source," Jpn. J. Appl. Phys., Part 1 **50**, 06GB09 (2011).
[36]S. Katsuki, A. Kimura, Y. Kondo, H. Horita, and T. Namihira, "Effects of an axial magnetic field on Z-pinch plasmas for extreme ultraviolet sources," J. Appl. Phys. **99**, 013305 (2006).